

High-Sensitivity Flexible Sensors Based on Island-Bridge Configuration for Real-Time Posture Monitoring Systems

Ning Ding, Yan Bai, Zhen You, Shiyan Wang, Longlu Wang, Weiwei Zhao,* Yuhui Feng, Feifei Lin, Yuzhe Chen, Xiang Zou, Xiaoyuan Jia, Mengyue Jiang, Wen Lv, Shujuan Liu, and Qiang Zhao*



Cite This: <https://doi.org/10.1021/acssensors.5c01118>



Read Online

ACCESS |

Metrics & More

Article Recommendations

Supporting Information

ABSTRACT: High-sensitivity, flexible sensors are crucial for precise posture monitoring in wearable electronics. Conventional single conductive network hydrogels suffer from limited strain-impedance response due to isolated conductive fillers. Herein, we propose a novel conjugative effect-assisted internal island-bridge mechanism to construct a sophisticated binary conductive network through $p-\pi$ stacking and electrostatic interaction between MXene islands and PEDOT:PSS bridges. This island-bridge configuration enables effective disruption and restoration during deformation, overcoming the limitations of single conductive networks. Optimized PVA/MXene/PEDOT:PSS (PMP) hydrogels achieve remarkable 188% increase in conductivity ($\sigma = 21.09 \text{ S cm}^{-1}$) and 98% improvement in sensitivity ($GF = 2.31$). This exceptional strain-impedance response allows for precise detection of complex joint movements. Furthermore, we developed a lightweight (31 g), low-power (40 mW) wearable posture monitoring system (WPMS) integrating PMP sensors with wireless communication modules for real-time health management through postural analysis and correction. This work presents a theoretical framework for designing high-sensitivity flexible sensors based on island-bridge configurations, advancing the intersection of healthcare and wearable electronics.

KEYWORDS: hydrogel sensor, conjugative effect, island-bridge configuration, wearable electronics, posture monitoring system



Flexible wearable electronics have emerged as promising platforms for diverse intelligent interaction scenarios, including sports analytics,^{1,2} human–computer interaction,^{3,4} and health monitoring systems.^{5,6} However, there still remains a critical demand for strain sensors that can effectively combine mechanical compatibility and biocompatibility with biological tissues, particularly for accurate monitoring of physiological signals in medical applications such as musculoskeletal disorders,⁷ rehabilitation,⁸ and injury prevention.⁹ Conductive hydrogels, known for their facile signal acquisition and manufacturing processes, have been widely utilized as resistive strain sensing layers and integrated with wireless communication modules for real-time posture monitoring.^{10,11} Among them, poly(vinyl alcohol) (PVA)/MXene hydrogels represent a promising candidate for wearable sensors, which combines the biocompatibility of PVA with the exceptional conductivity of $Ti_3C_2T_x$ MXene.¹² The interfacial interactions via hydrogen bonding between the hydrophilic surface groups (i.e., $-OH$, $-O-$, $-F$) of MXene nanosheets and $-OH$ groups in PVA chains not only ensure uniform dispersion of the nanosheets within the hydrogel matrix but also enhance load transfer and energy dissipation under tensile forces.¹³ However, the negatively charged surface groups induce electrostatic repulsion between the nanosheets, which results in isolated conductive islands that disrupt electron transmission channels, thus leading to suboptimal conductivity and sensing proper-

ties.¹⁴ Although increasing MXene content can marginally improve these properties, excessive amounts impede the effective sliding of polymer chains, which significantly compromises the mechanical properties.^{15,16}

The island-bridge configuration, typically composed of anchored rigid islands and slippable flexible bridges, has the potential to advance the sensitivity of strain sensors for stretchable electronics.¹⁷ The construction of binary conductive networks through interface interactions presents a promising approach to bridge conductive islands without compromising the mechanical properties. More importantly, this design inspires us to overcome the electrostatic repulsion caused by surface electronegativity through interface interactions, which may connect MXene to specific conductive materials to form a robust electronic transport channel. Notably, poly(3,4-ethylenedioxythiophene):poly(styrenesulfonate) (PEDOT:PSS), with its conducting PEDOT cations and insulating PSS anions, features a distinctive long and flexible polymer chain structure that

Received: April 4, 2025

Revised: July 9, 2025

Accepted: July 14, 2025

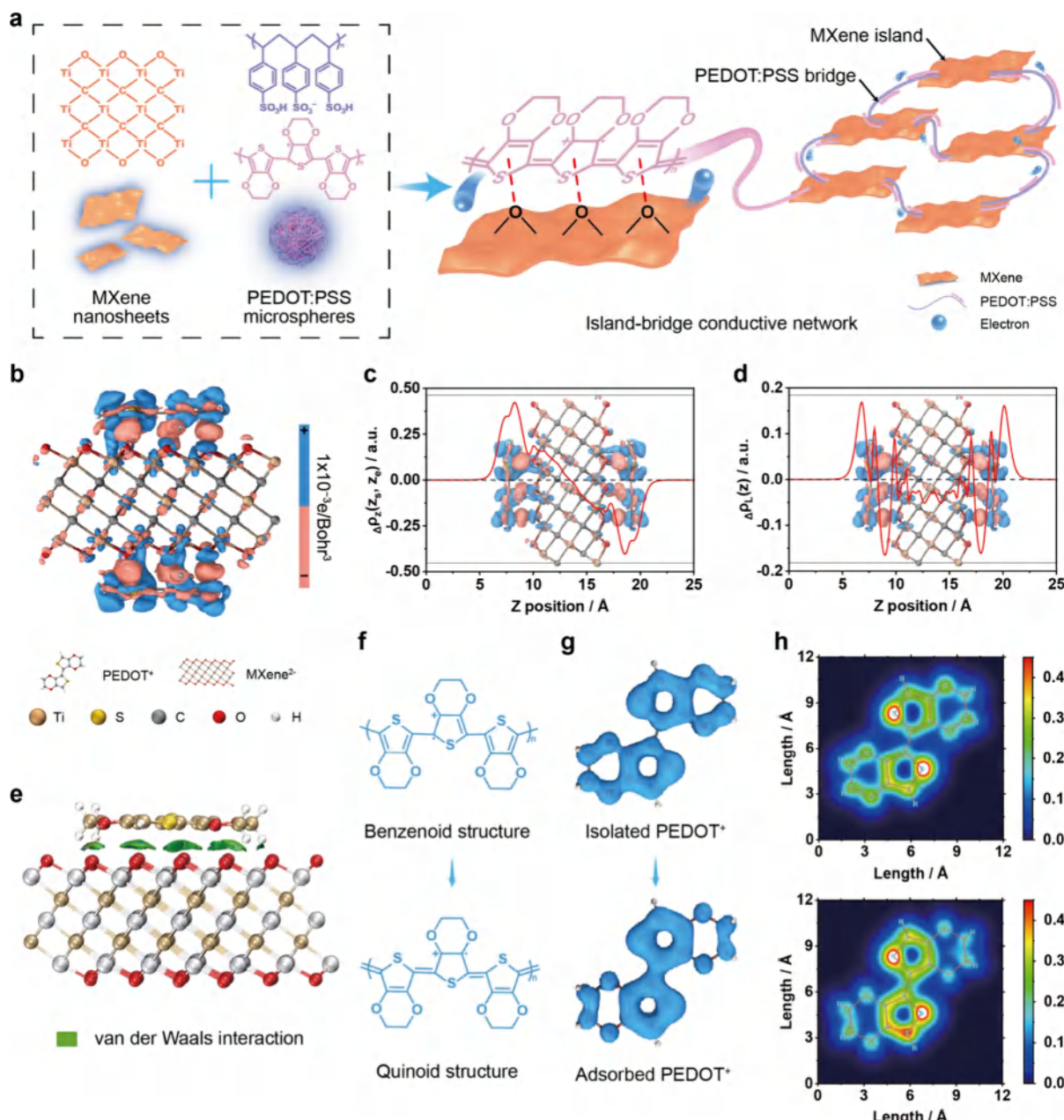


Figure 1. Design of PMP hydrogels. (a) Schematic diagram of the conjugative effect-assisted internal island-bridge mechanism. (b) Side view of EDD for the interfaces between PEDOT and MXene ($Ti_3C_2O_2$). (c) Charge displacement curve in the Z direction. (d) Local integral curve of EDD in the Z direction. (e) IGMH analysis for the p- π stacking between MXene and PEDOT. (f) Structural formulas for the benzenoid and quinoid structures of PEDOT. (g) Isosurface of LOL- π for the isolated and adsorbed PEDOT⁺. (h) Color-filled maps of LOL- π at 0.75 Å above isolated and adsorbed PEDOT⁺.

emerges as a promising candidate to bridge MXene nanosheets.¹⁸ In addition, it can also uniformly disperse within the hydrogel framework through the hydrogen bond interactions with PVA chains, which facilitate excellent mechanical properties and biocompatibility. However, PEDOT:PSS tends to form micelle microspheres with PEDOT-rich cores and PSS-rich shells in aqueous solution, which creates a negative surface charge and hinders the formation of a continuous conductive network.^{19,20} In theory, PEDOT can tightly adsorb onto MXene surfaces due to the interactions between surface functional groups.²¹ Nevertheless, the underlying mechanism driving the microstructure transformation and conductive behavior of PEDOT has not been reported. It

is highly desirable to unravel the intricate relationship between the polymer morphology and electrical conductivity of PEDOT, which provides a robust theoretical foundation for advancing highly sensitive PEDOT:PSS-based sensors with precisely engineered strain-impedance-responsive conductive networks.

In this work, we propose a novel conjugative effect-assisted internal island-bridge mechanism to construct an island-bridge structure within the binary conductive network in the PVA/MXene/PEDOT:PSS (PMP) hydrogel through p- π stacking and electrostatic interaction (Figure 1a). The transformation of π electron conformation from benzoid to quinoid structure results in long-range conjugative PEDOT chains, which

promotes the change from curved structure to linear structure, and reveals the conjugative effect-assisted internal island-bridge mechanism to achieve the phase separation of core–shell PEDOT:PSS. Consequently, the efficient electron transfer process through the binary conductive network contributes to a nearly 3-fold increase in conductivity (21.09 S cm^{-1}) compared to PVA/MXene (PM) hydrogel with isolated conductive islands. Under mechanical strain, the controlled disruption of PEDOT-MXene interfacial interactions leads to a systematic breakdown of the binary conductive network within the island-bridge architecture, thus resulting in an exceptional strain-impedance response (gauge factor, GF = 2.31) for the PMP sensing layer. Accordingly, PMP sensors show high-sensitivity signal acquisition capabilities in the intelligent real-time wearable posture monitoring system (WPMS) for comprehensive health management applications. This innovative conjugative effect-assisted island-bridge mechanism provides a theoretical framework for the rational design and synthesis of hydrogels incorporating multiple conductive components, which offers a new paradigm for advancing high-sensitivity flexible sensors with transformative potential in the field of healthcare and wearable electronics.

RESULTS

Design of PMP Hydrogels. The PMP hydrogel is synthesized by incorporating MXene nanosheets and PEDOT:PSS into the PVA matrix with sodium tetraborate as a cross-linking agent (Figures S1–S3). The chemically cross-linked network is formed through the formation of reversible borate ester bonds between the hydroxyl groups ($-\text{OH}$) in PVA and the tetraborate ions ($\text{B}(\text{OH})_4^-$). The physically cross-linked network is constructed through the formation of hydrogen bonds between $-\text{OH}$ groups in PVA, sulfonic acid groups ($-\text{SO}_3\text{H}$) in PEDOT:PSS, and rich hydrophilic surface groups (i.e., $-\text{OH}$, $-\text{O}$, $-\text{F}$) in MXene. The electrostatic forces between electronegative MXene and positively charged PEDOT chains ensure the stable dispersion of MXene as well as establish efficient conductive channels in the PMP hydrogel.²² They can be elongated up to seven times their original length, which demonstrates excellent stretchability for practical applications (Figure S4). Additionally, the PMP hydrogel displays notable plasticity and can be molded into various shapes, including circles, flowers, stars, hearts, and letters, which provides essential mechanical properties for subsequent device applications (Figure S5).

To gain a deeper insight into the interaction mechanism between MXene and PEDOT, density functional theory (DFT) calculations have been conducted to explore the interaction mechanism and investigate the conformational transition of PEDOT (Figure S6). PVA is omitted from the conductivity analysis as such insulating polymer functions solely as the structural scaffold for the binary conductive network without influencing the charge transfer between conductive units.²³ The electron transfer between MXene and PEDOT is investigated through electron density difference (EDD) analysis. Figure 1b illustrates that the red charge depletion regions are predominantly dispersed across the MXene^{2-} sheet, whereas the blue charge accumulation areas encircle the PEDOT^+ units. This result suggests the existence of an effective charge transfer between MXene and PEDOT.²⁴ Charge displacement analysis along the Z-axis reveals a net transfer of 0.42 electron from MXene^{2-} to each PEDOT^+ unit, when the interfaces between MXene^{2-} and PEDOT^+ are

assumed at $Z = 8.24$ and 18.56 \AA , respectively (Figure 1c). The local integral curve of density difference along the Z direction reveals that the transferred electrons are distributed on both sides of the molecular plane of PEDOT^+ (Figure 1d). Moreover, the independent gradient model based on Hirshfeld partition (IGMH) analysis is performed to analyze the $p-\pi$ stacking between MXene and PEDOT. As illustrated in Figure 1e, the green isosurface depicts the van der Waals interactions between the fragments, which in this case represents the $p-\pi$ interaction between the p orbitals of the terminal $-\text{O}$ groups on the MXene surface and the π orbitals of PEDOT. Such $p-\pi$ interaction, coupled with the charge transfer between MXene and PEDOT, effectively promotes the π -electron delocalization along the PEDOT polymer chains and results in a conformational change from a benzenoid to quinonoid structure (Figure 1f).²⁵ The isosurface of the localized orbital locator based on π molecular orbitals (LOL- π) clearly depicts the global delocalization channels of the electrons in π molecular orbitals (Figure 1g). Upon adsorption, the isosurface reconfigures, which localizes around the thiophene ring and establishes connectivity between two monomers along the C–C bond, thereby enhancing the delocalization of π electrons. To better visualize the distribution of LOL- π , color-filled maps are plotted at 0.75 \AA above PEDOT^+ and on the vertical plane along the C–C bond connecting the two monomers (Figure 1h and Figure S7). Notably, the π electron density on the five-membered thiophene ring, especially along the C–C bond connecting EDOT monomers, increases significantly after the adsorption of PEDOT^+ to MXene^{2-} . Moreover, the same delocalization of the π electron is observed in the asymmetric adsorption model (Figures S8 and S9). This interaction induces a conformational change in PEDOT chains from a coil-like benzoid structure in their pristine state to a linear-like quinoid structure. The long-range π -electron conjugative effect along the PEDOT chains facilitates their transformation from a curved structure to a linear conformation. Concurrently, electrostatic interactions between MXene and PEDOT disrupt the electrostatic balance within the PEDOT:PSS complex. Coupled with the conformational change, these interactions promote physical connections between PEDOT domains, leading to phase separation of PEDOT:PSS. Consequently, PEDOT:PSS undergoes transitions from a disordered core–shell structure to an extended conductive fiber morphology, thereby contributing to the formation of a highly continuous MXene-PEDOT conductive network. These results comprehensively confirm the conjugative effect-assisted internal island-bridge mechanism, which will form the foundation for high-sensitivity strain sensors.

The microstructure and elemental composition of the PMP hydrogel are further characterized by scanning electron microscopy (SEM) and energy-dispersive X-ray spectroscopy (EDS). SEM image reveals the characteristic 3D porous network structure through the incorporation of MXene and PEDOT:PSS into the PVA matrix (Figure S10a). Meanwhile, EDS elemental mapping confirms the uniform dispersion of Ti, O, F, and S elements in the PMP hydrogels, indicating the homogeneous distribution of MXene nanosheets and PEDOT:PSS in the PVA matrix (Figure S10b). To reveal the interactions among PVA, MXene, and PEDOT:PSS, Fourier transform infrared (FT-IR) spectra of PVA, PM, and PMP hydrogels are obtained as shown in Figure S11a. The distinct peaks at 1422 and 1347 cm^{-1} in hydrogels are assigned to asymmetric stretching vibration of the newly formed $\text{B}-\text{O}-\text{C}$

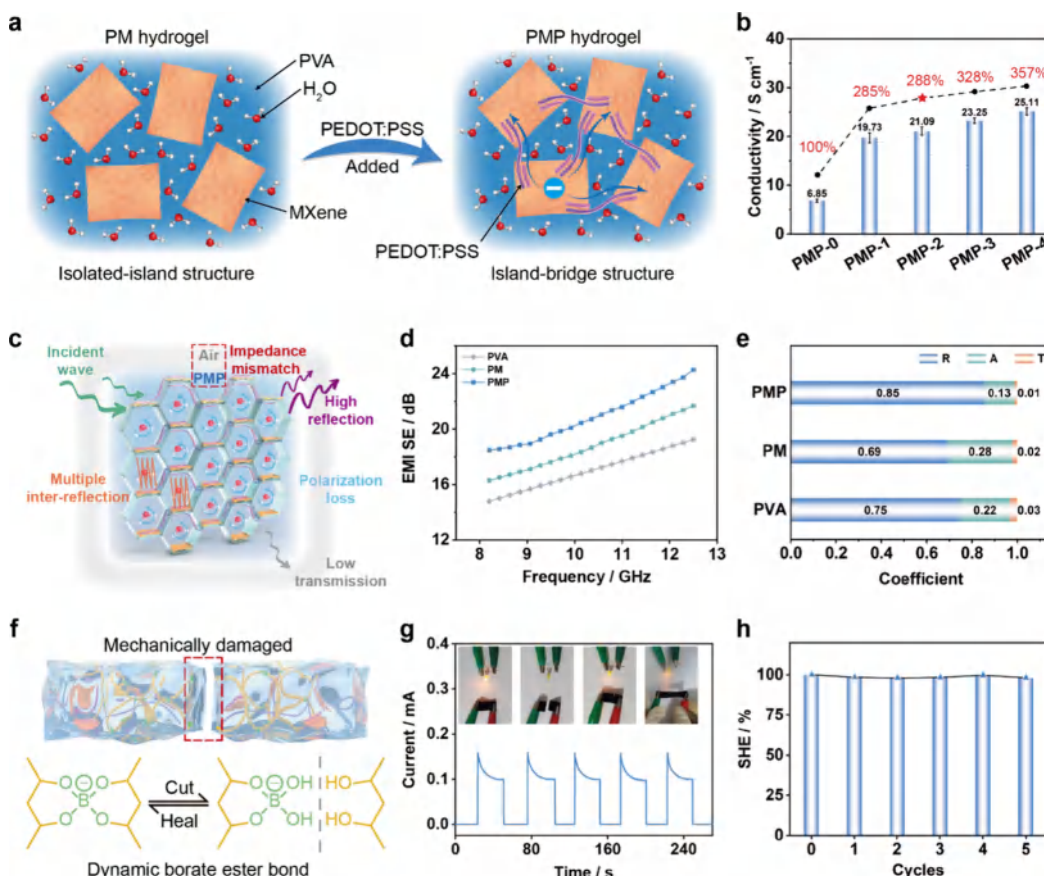


Figure 2. Properties of PMP hydrogels. (a) Schematic diagram of isolated-island structure in PM hydrogels and island-bridge structure in PMP hydrogels. (b) Conductivity of PMP hydrogels with different contents of PEDOT:PSS (the line graph represents the change rate of conductivity for PMP hydrogels compared to PM hydrogels). (c) EMI shielding mechanism of PMP hydrogels. (d) EMI SE_T plots in the X-band (8.2–12.4 GHz) and (e) R, A, and T coefficients of PVA, PM, and PMP hydrogels. (f) Schematic illustration of the self-healing property of PMP hydrogels with the reversible borate ester bonds between PVA chains and borax. (g) Current change curves of the PMP hydrogel in five consecutive cut-healing cycles and photographs of yellow LED brightness lit by the PMP hydrogel in different states (i.e., original, cut, healing, and stretching after healing). (h) Average self-healing efficiency of PMP hydrogels for different healing times.

bond between PVA chains and $\text{B}(\text{OH})_4^-$, which confirms the successful chemical cross-linking of PVA and lays a foundation for the excellent self-healing ability of PMP hydrogels.²⁶ The peak at 511 cm^{-1} is attributed to the stretching vibration of the $\text{Ti}-\text{O}-\text{Ti}$ bond, which confirms the introduction of MXene. It exhibits a blue shift compared with that of MXene nanosheets, which is ascribed to the strong hydrogen-bonding interactions between terminal groups ($-\text{O}$, $-\text{OH}$) of MXene and $-\text{OH}$ groups of PVA (Figure S11b).²⁷ Moreover, the new characteristic peak at 1155 cm^{-1} in the spectrum of PMP hydrogels is attributed to the $\text{S}-\text{O}$ bond of the sulfonic acid group in PSS. It exhibits a slight blue shift compared with that of PEDOT:PSS, which confirms the hydrogen-bonding interactions between the $-\text{SO}_3\text{H}$ groups and $-\text{OH}$ groups of PVA (Figure S11b).²⁸ Moreover, Raman spectral analysis reveals the conformational transformation of PEDOT from benzoid to quinoid within PMP hydrogels (Figure S12). This observation confirms the phase separation of PEDOT:PSS, which transitions from a disordered core-shell structure to an extended conductive fiber morphology, thereby contributing to the formation of a highly continuous island-bridge conductive network with MXene islands and PEDOT bridges.

Properties of PMP Hydrogels. To further elucidate the effect of the island-bridge configuration on the properties of hydrogels, the electrical and mechanical characteristics of

hydrogels with different MXene contents and PEDOT:PSS contents have been systematically investigated. For PM hydrogels, as the incorporation of MXene nanosheets increases from 0 to 5 mg into PVA matrix, the electrical conductivity is significantly boosted from 2×10^{-2} to 2.22 S cm^{-1} , and tensile strength rises from 22.33 to 53.88 kPa due to a denser conductive network and reinforced hydrogen-bonded structure (Figure S13 and Table S1). Considering that excessive MXene hinders the effective slip of PVA chains, which results in a reduction in tensile fracture strain, the content of MXene in the hydrogel is selected to be 7 mg (PMP-0).²⁹ The further incorporation of the conductive polymer PEDOT:PSS into PMP-0 leads to the development of an island-bridge structure in the PMP hydrogel, which notably enhances its electrical and mechanical properties (Figure 2a and Table S2). Significantly, the conductivity of PMP-1 exhibits a dramatic increase and reaches approximately 2.9 times that of PMP-0. This significant enhancement is observed with the addition of only 0.02 wt % PEDOT:PSS, which results not merely from the parallel connection of MXene and PEDOT but also from the efficient charge transfer between two conductive units through the conjugative effect-assisted internal island-bridge network with MXene islands and PEDOT bridges (Figure 2b). It is important to note that a small amount of PEDOT:PSS (0.02 wt %) is sufficient to connect most of the dispersed MXene

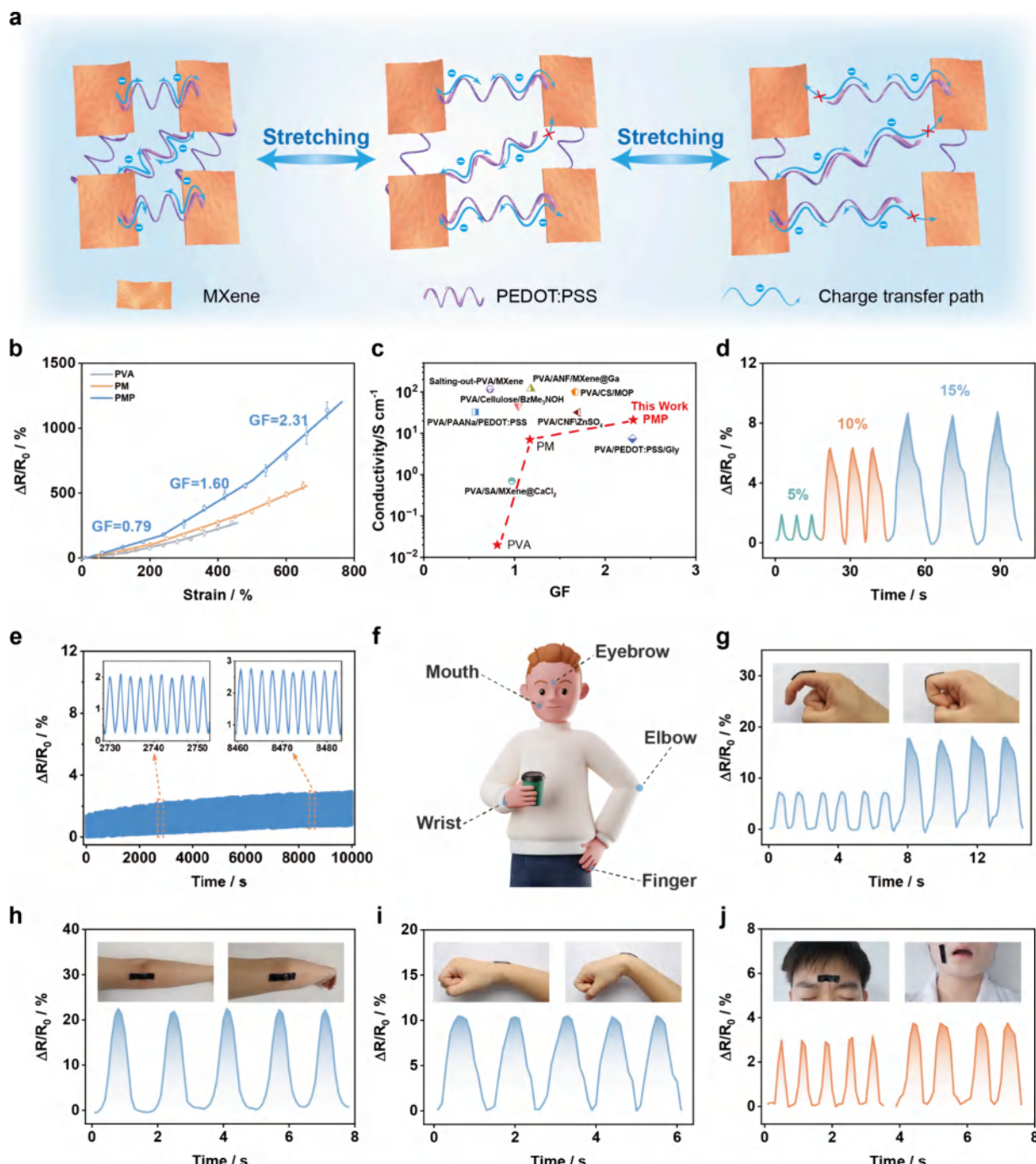


Figure 3. Sensing performance of PMP hydrogel strain sensors. (a) Schematic diagram of the response mechanism for PMP hydrogel sensors. (b) Relative resistance variation at different strains. (c) Comparison between hydrogel sensors in this work and previously reported PVA-based hydrogel strain sensors in conductivity and strain GF values. A detailed description of each data point is presented in Table S3. (d) Relative resistance variation under different strains (i.e., 4, 10, and 15%). (e) Relative resistance stability in 10,000 s at a strain of 4%. (f) Schematic of moving parts of the human body that can be monitored. Real-time recording of the relative resistance changes generated by various human activities of (g) the finger, (h) the elbow, (i) the wrist, (j) the eyebrow, and the mouth.

nanosheets. Therefore, further addition of PEDOT:PSS moderately increases conductive pathways within the existing networks, leading to a 27% enhancement in conductivity as the addition amount increases from 0.02 to 0.05 wt %. Considering the optimal combination of mechanical properties and electrical conductivity, the PMP-2 hydrogel with 0.03 wt % PEDOT:PSS is chosen for further performance evaluation, exhibiting a tensile strength of 93.57 kPa and a fracture strain of 785% (Figure S14).

The leap in the conductivity of PMP hydrogels resulting from the island-bridge conductive network is further confirmed by electromagnetic interference (EMI) shielding applications (Figure 2c and Figure S15). The PMP hydrogel has an EMI shielding efficiency (SE) of 24.3 dB at 12.4 GHz, which is significantly better than 21.7 dB of the PM hydrogel and 19.2 dB of the PVA hydrogel (Figure 2d and Figure S16). A reduction in transmissivity (T) corroborates the gradual enhanced EMI SE, with PMP hydrogels showing the lowest

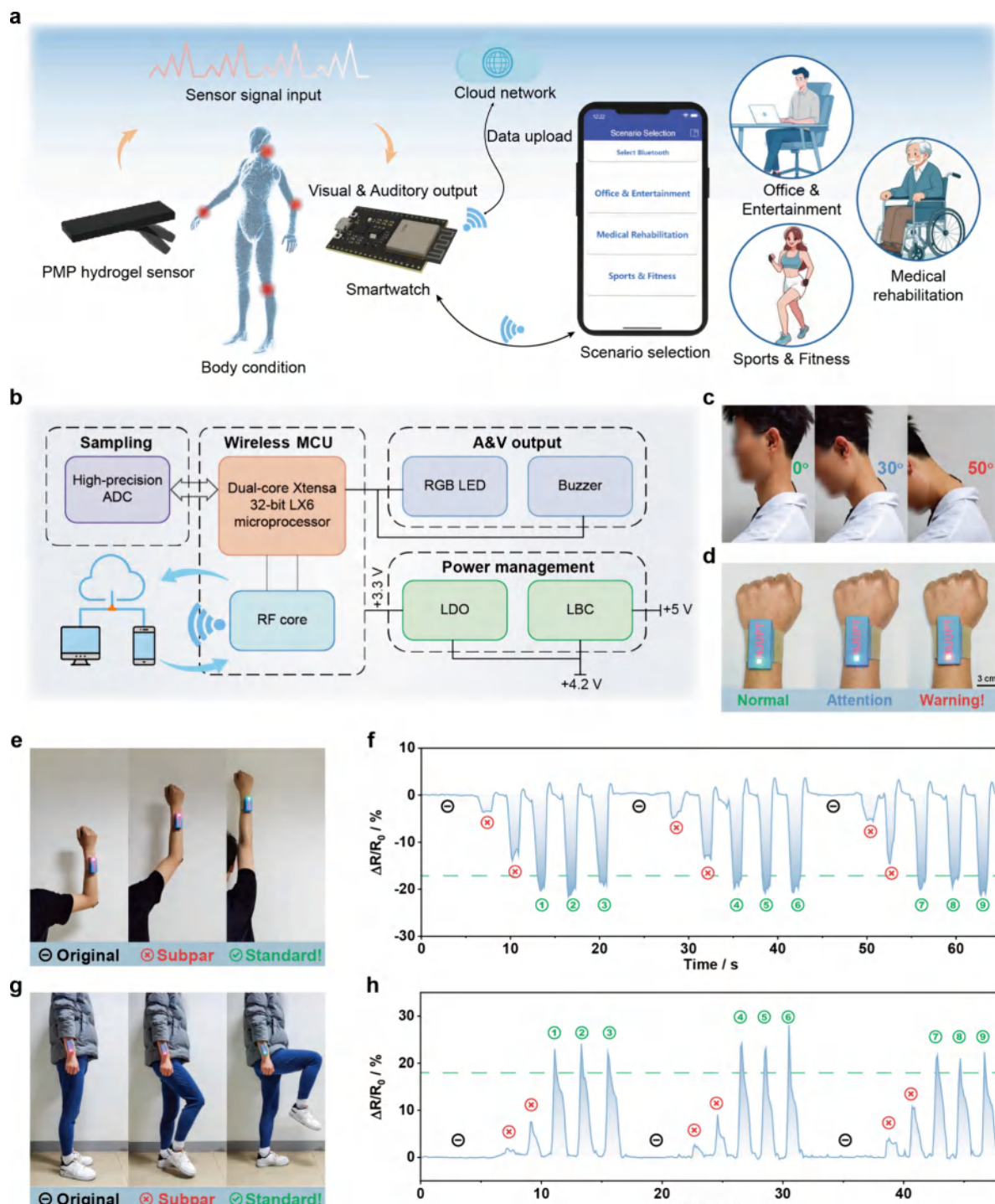


Figure 4. Application of PMP hydrogels. (a) Schematic diagram of WPMS to monitor the postures of the physical body. (b) Brief block diagram of the WPMS. (c) Photographs of PMP hydrogel sensor attached to the neck under different neck bending angles (i.e., 10, 30, and 50°). (d) Photographs of RGB LED on the smartwatch under normal, attention, and warning states. (e) Photographs of the PMP hydrogel sensor attached to the elbow and corresponding RGB LED on the smartwatch under different states (i.e., original, subpar, and standard) for arm medical rehabilitation. (f) Relative resistance variation of the PMP hydrogel sensor during 15 arm flexion and extension cycles for arm medical rehabilitation. (g) Photographs of the PMP hydrogel sensor attached to the knee and corresponding RGB LED on the smartwatch under different states (i.e., original, subpar, and standard) for high knees. (h) Relative resistance variation of the PMP hydrogel sensor during 15 cycles of high knees exercise.

T, followed by PM hydrogels, and then PVA hydrogels (Figure 2e). To be specific, an elevation in absorptivity (A) coupled with a diminution in reflectivity (R) for the PM hydrogel suggests that the incorporation of MXene primarily augments the internal electromagnetic reflection and absorption of the

hydrogels. Conversely, the PMP hydrogel exhibits a marked decrease in A and a concurrent rise in R, which indicate a significant enhancement in the impedance mismatching between the hydrogel surface and air. This observation aligns with the conductivity enhancement engendered by the island-

bridge conductive network of self-assembled MXene and PEDOT. Moreover, the 5 mm-thick PMP hydrogel has the EMI SE of 35.5 dB at 12.4 GHz, equating to a 99.67% blockage of incident waves, which is a promising candidate for next-generation EMI shielding materials (Figure S17). The outstanding EMI shielding performance of PMP hydrogels further confirms the presence of a binary conducting network within the PVA polymer skeleton, which establishes a robust foundation for their excellent sensing capabilities.

The self-healing capability of hydrogel sensors is essential to achieving long-term stability of flexible wearable posture monitoring systems.³⁰ PMP hydrogels exhibit remarkable self-healing ability due to the reversible borate ester bond between the hydroxyl group of PVA and $B(OH)_4^-$ in the 3D polymer network (Figure 2f).³¹ The self-healing process of the PMP hydrogel is visually demonstrated with a yellow light-emitting diode (LED) that serves as an indicator, and the corresponding circuit diagrams are depicted in Figure S18. Upon rejoining the segments of the severed PMP hydrogel, its self-healing properties are activated, which promptly restore illumination to the LED and repair the circuit (Figure 2g). Notably, the LED indicator remains lit when the healed hydrogel is stretched, which indicates the synchronous restoration of the mechanical properties of the hydrogel. Specifically, the self-healed PMP hydrogel demonstrates an exceptional mechanical self-healing efficiency of 93.12% (Figure S19). The real-time changes in current during five cut-healing cycles record the self-healing process of PMP hydrogels. The current drops to zero when the hydrogel is cut off but rapidly increases when the separated hydrogel segments are reconnected and gradually returns to the initial state within 20 s (Figure S20). Remarkably, the current changes consistently exhibit a high degree of consistency across five consecutive cut-healing cycles, with an average electrical self-healing efficiency (SHE) of 98.43% evaluated in terms of conductivity, which is attributed to the reversible destructibility of the internal island-bridged conductive network (Figure 2h). This remarkable combination of mechanical and electrical self-healing abilities ensures the prolonged reliability and service life of PMP hydrogels and opens avenues for their application in WPMS. The biocompatibility and noncytotoxicity of PMP hydrogels have been confirmed, which are fundamental to their suitability and safety in wearable hydrogel sensors intended for human use, making them a safe option for WPMS (Figure S21).

Sensing Performance of PMP Hydrogels. Based on the comprehensive properties mentioned above, a PMP hydrogel-based flexible strain sensor is explored to detect and collect human health parameters. Such sensors are expected to have an outstanding strain-impedance response due to the deformation-induced separation between conductive units, which alters the structure of the island-bridge conductive network and significantly changes the relative resistance (Figure 3a). Specifically, under minor strain, numerous PEDOT:PSS interconnections undergo slippage and subsequent dissociation, which reduce the cross-linking density of the conductive network and progressively increase the electrical resistance. Furthermore, under substantial strain, the $p-\pi$ stacking between MXene and PEDOT:PSS is disrupted by external forces, which precipitate the disjunction of the island-bridge configuration and culminate in a pronounced diminution of the conductive pathways and a swift surge in resistance. As a result, the PMP sensor exhibits a

GF of 0.79 in the strain range of 0–238%, 1.60 in the strain range of 238–498%, and 2.31 in the strain range of 498–763% (Figure 3b). The GF for PMP hydrogels exhibits a remarkable 98% increase due to the synergistic effect of MXene and PEDOT:PSS, which significantly outperforms the 10% increase observed in PM hydrogels with MXene alone. Compared to previously reported PVA-based hydrogels, the PMP hydrogel developed in this work exhibits superior conductivity and strain sensitivity, which underscore the effectiveness of the island-bridge structure (Figure 3c). The relative resistance change of the sensor increases with the increased applied tensile strain and remains stable during three consecutive strain cycles, which indicates its capability to monitor various levels of tensile strain (Figure 3d). Moreover, the relative resistance change of the sensor remains constant throughout the 10,000 s cycle stability test, demonstrating great repeatability (Figure 3e).

Given the excellent mechanical properties, sensing properties, and biocompatibility of the PMP hydrogel, it can serve as a wearable strain sensor for monitoring human physiological activities (Figure 3f). It is worth noting that the PMP hydrogel does not pose a risk of bioelectric stimulation or thermal effect, making it suitable as a safe and reliable material for wearable flexible sensors (Figures S22 and S23). The PMP sensor demonstrates an effective responsiveness to the corresponding movements when attached to various joints (Figure 3g–i). Specifically, the PMP sensor accurately detects relative resistance changes with fingers, wrists, and elbows at a certain bending angle and exhibits a consistent and repeatable signal output in several continuous tests. Notably, as the bending angle of the index finger increases from 45 to 90°, the relative resistance change of the sensor also increases, which demonstrates the potential of sensors to accurately feedback the specific bending angle of joints (Figure 3g). Additionally, when the PMP sensor is attached to the corners of the mouth or eyebrows, the relative resistance repeatedly changes under facial actions, such as smiling or frowning, which indicates the potential for facial expression recognition (Figure 3j). Moreover, the response time and recovery time of the PMP hydrogel strain sensor were measured to be 381 and 341 ms, respectively (Figure S24). The accurate and sensitive sensing response of the PMP hydrogel opens avenues for applications in WPMS, which showcases its potential impact on the future of personalized healthcare.

Application of the Posture Monitoring System. A novel WPMS is developed through utilizing PMP hydrogels as the sensing materials, with the goal of comprehensive monitoring, prompting, and correcting the physical state of the human body in various scenarios. The working schematic diagram and concise block diagram of WPMS to monitor the postures of physical body are depicted in Figure 4a and Figure 4b, respectively. PMP sensors are strategically positioned across various body joints, including the cervical spine, wrists, elbows, and knees, which enables the collection of resistance signal data corresponding to joint movements. Before transmission to the microcontroller, the original data is converted into digital signals by a 12-bit high-precision analog-to-digital converter. The microcontroller unit (MCU) remaps the data at a high sampling frequency of 50 Hz and then determines the current joint state by comparing it with the preset threshold, which ensures the real-time performance of the monitoring. Dual signals (visual and auditory, V&A) are output through the RGB LED and the buzzer to prompt the posture.

Noteworthy is the embedded Bluetooth Low Energy (BLE), which allows users to seamlessly switch between different WPMS application scenarios with a simple click on the mobile graphical user interface (GUI). Additionally, through wireless fidelity (WIFI) technology, the monitoring data from the smartwatch is uploaded to the cloud network in real time for further processing and analysis. The WPMS works with low power consumption (40 mW) and is powered by a rechargeable lithium-ion battery (200 mAh) through a low dropout linear voltage regulator (LDO) stabilized at 3.3 V. All electronic components, including wireless MCU, RGB LED, buzzer, rechargeable lithium-ion battery, and linear battery charger (LBC), are encapsulated in a lightweight (31 g) wearable smartwatch (**Figures S25–S28**).

Humans frequently tilt their heads toward screens during daily activities, contributing to forward-head posture (FHP), which disrupts the “neutral spine” alignment and can lead to muscle strain, cervical disc degeneration, pain, and neurological disorders.³² To address this, timely reminders and corrections are crucial. The sensor attached to the cervical spine monitors the head-bending angle and categorizes responses into three intervals: normal, attention, and warning (**Figure 4c** and **Figures S29 and S30**). The smartwatch emits corresponding LED responses and alarm sounds to prompt posture correction, particularly when the head-bending angle is excessive (**Figure 4d** and **SI Movie S1**). Similarly, the system monitors wrist posture during writing, preventing soreness and muscle strain (**SI Movie S2**). Moreover, for individuals undergoing physical recovery, the WPMS supervises repetitive exercises for patients with arm injuries, providing guidance and prompts (**SI Movie S3**). It evaluates elbow movements: if the elbow remains bent and the sensor signal does not reach the threshold, the smartwatch emits a red LED light; if fully extended, a green LED light and buzzer indicate a standard movement (**Figure 4e,f**). Additionally, fitness enthusiasts benefit from real-time feedback on leg raises through knee-attached sensors (**SI Movie S4**). If the knee fails to bend to a 90° angle during high leg raises, a red LED light indicates a subpar performance. Conversely, a green LED light indicates a standard movement when the knee reaches the angle (**Figure 4g,h**). The WPMS uploads real-time statistics to the cloud via WIFI for remote analysis and feedback by users or experts, which further enhances the practicality of the system (**Figures S31–S33**). In conclusion, WPMS based on PMP hydrogels empowers users to monitor their physical state independently, demonstrating extraordinary application potential in posture monitoring, medical rehabilitation, and sports fitness.

CONCLUSIONS

In summary, we propose a novel conjugative effect-assisted internal island-bridge mechanism to construct a binary conductive network in PMP hydrogels, which enhances the strain-impedance response as well as leverages p–π stacking and electrostatic interaction. Theoretical calculations reveal that transformation of the π electron conformation in PEDOT can induce a structural transition from a curved to a linear polymer configuration, thereby achieving the phase separation of core–shell PEDOT:PSS and establishing the long-range conjugative PEDOT chain as an effective bridging linkage for MXene. As a result, the PMP sensor exhibits a significantly improved strain-impedance response for enhanced sensitivity by 98% (GF = 2.31), thus enabling precise detection of human movements across multiple joints. The pioneering PMP

WPMS further empowers users to actively monitor and receive real-time feedback on their physical posture, which demonstrates substantial potential across a spectrum of scenarios. This work provides a theoretical island-bridge framework for the rational design and synthesis of high-sensitivity flexible sensors and further paves the way for the transformative intersection of healthcare and wearable electronics.

MATERIALS AND METHODS

Materials. Ti_3AlC_2 powder (>99.9 wt %) was purchased from 11 Technology Co., Ltd. Hydrochloric acid (HCl, 37 wt %) was procured from Sinopharm Chemical Reagent Co., Ltd. Lithium fluoride (LiF, >99%) and poly(vinyl alcohol) (PVA, 98–99%) were obtained from Shanghai Aladdin Biochemical Technology Co., Ltd. Anhydrous sodium tetraborate (borax, >99.5%) was purchased from Sun Chemical Technology (Shanghai) Co., Ltd. Poly(3,4-ethylenedioxythiophene):polystyrenesulfonate (PEDOT:PSS, 1.0–1.3%) was purchased from Xi'an Function Material Group Co., Ltd. Dulbecco's modified Eagle's medium (DMEM), MTT, and the live-dead cell staining kit were supplied by Jiangsu KeyGEN Biotechnology Co., Ltd. All the chemicals were used as received without further purification. Deionized water was purged with argon for 15 min to remove dissolved oxygen before use.

Preparation of $Ti_3C_2T_x$ MXene Nanosheets. MXene nanosheets were prepared by selectively etching the Al layer from Ti_3AlC_2 bulks using a modified LiF/HCl etching method, as described in the previous work.³³ To be specific, the etchant was prepared by adding 0.5 g of LiF to 10 mL of HCl (9 M) and then stirring for 20 min. Subsequently, 0.5 g of Ti_3AlC_2 powder was slowly added to the etchant, and the stirring was continued for 30 min. Then, the mixture was heated to 60 °C for 24 h. Afterward, the products were centrifuged at 3500 rpm several times with deionized water until the pH exceeded 6 and then dried under a vacuum for 12 h. Next, 0.14 g of multilayer MXene was dispersed in 7 mL of deionized water and sonicated (60 kHz, 360 W) under an argon flow for 1 h to obtain MXene nanosheets. Finally, after centrifugation at 3500 rpm for 1 h, an aqueous dispersion of MXene nanosheets was collected.

Synthesis of PVA Hydrogels. The PVA hydrogels were synthesized by preparing a PVA solution with a concentration of 10 wt %. Initially, 0.2 g of PVA was dissolved in 1.865 mL of deionized water under continuous mechanical stirring at 95 °C for 2 h, rendering a visually transparent solution (abbreviated as solution P). Subsequently, 0.4 g of anhydrous sodium tetraborate powder was introduced into a separate glass bottle containing 6.25 mL of deionized water, and then the mixture was stirred at 80 °C for 1 h. Finally, the prepared sodium tetraborate solution (abbreviated as solution B) was combined with the P solution, culminating in the formation of the PVA hydrogel.

Synthesis of PM Hydrogels. Initially, the MXene dispersion was added to cooled solution P and continuously stirred for 2 h. Subsequently, solution B was introduced into the combined solution of MXene and PVA, resulting in the formation of the PM hydrogel. Diverse quantities of MXene (i.e., 0, 3, 5, 7, and 10 mg) were utilized to synthesize distinct PM hydrogels, denoted as PM-0, PM-3, PM-5, PM-7, and PM-10, respectively.

Synthesis of PMP Hydrogels. Initially, the MXene dispersion and PEDOT:PSS solution were added to cooled solution P and continuously stirred for 2 h. Subsequently, solution B was introduced into the combined mixture of MXene, PEDOT:PSS, and PVA, leading to the successful formation of the PMP hydrogel. To synthesize distinct PMP hydrogels, the same quantity of MXene (7 mg) was utilized, while the amounts of PEDOT:PSS were systematically employed as 0, 0.4, 0.65, 0.9, and 1.1 mL. Correspondingly, the as-resulted hydrogels were denoted as PMP-0, PMP-1, PMP-2, PMP-3, and PMP-4, respectively.

Characterization. The morphology and microstructure of samples were characterized by SEM (Hitachi S-4800) and transmission electron microscopy (TEM, Tecnai G2 F30 S-TWIN at 200 kV). The elemental compositions were determined using EDS

(Horiba EX-250). X-ray diffraction (XRD) patterns were obtained using an X-ray diffractometer (Bruker AXS D8 Advance) using Cu K α radiation ($\lambda = 1.5418 \text{ \AA}$). FT-IR spectra were obtained by using an FT-IR spectrometer (PerkinElmer, PE-Spectrum Two). Raman spectra were obtained with a Raman spectrometer (Renishaw inVia) at a laser wavelength of 785 nm. To facilitate SEM observation, PMP hydrogels were subjected to freeze-drying treatment for 3 days using a freeze-drying machine (BILON FD-1A-50) and sputter-coating with gold on the surface to eliminate charging effects. To facilitate FT-IR characterization, the samples were dried and ground into powder under an infrared heat lamp.

■ ASSOCIATED CONTENT

§ Supporting Information

The Supporting Information is available free of charge at <https://pubs.acs.org/doi/10.1021/acssensors.Sc01118>.

Movie S1: Real-time monitoring system for cervical spine health ([MP4](#))

Movie S2: Real-time monitoring system for wrist health ([MP4](#))

Movie S3: Real-time monitoring system for medical rehabilitation ([MP4](#))

Movie S4: Real-time monitoring system for sports and fitness ([MP4](#))

Additional characterization, computational and experimental details (Figures S1–S33), and properties and composition of different hydrogels (Tables S1–S4) ([PDF](#))

■ AUTHOR INFORMATION

Corresponding Authors

Weiwei Zhao – State Key Laboratory of Flexible Electronics (LoFE) & Institute of Advanced Materials (IAM), Nanjing University of Posts & Telecommunications (NUPT), Nanjing 210023, China;  orcid.org/0000-0003-2926-8476; Email: iamwwzhao@njupt.edu.cn

Qiang Zhao – State Key Laboratory of Flexible Electronics (LoFE) & Institute of Advanced Materials (IAM) and College of Electronic and Optical Engineering & College of Flexible Electronics (Future Technology), Nanjing University of Posts & Telecommunications (NUPT), Nanjing 210023, China;  orcid.org/0000-0002-3788-4757; Email: iamqzhao@njupt.edu.cn

Authors

Ning Ding – State Key Laboratory of Flexible Electronics (LoFE) & Institute of Advanced Materials (IAM), Nanjing University of Posts & Telecommunications (NUPT), Nanjing 210023, China

Yan Bai – State Key Laboratory of Flexible Electronics (LoFE) & Institute of Advanced Materials (IAM), Nanjing University of Posts & Telecommunications (NUPT), Nanjing 210023, China

Zhen You – State Key Laboratory of Flexible Electronics (LoFE) & Institute of Advanced Materials (IAM), Nanjing University of Posts & Telecommunications (NUPT), Nanjing 210023, China

Shiyan Wang – College of Electronic and Optical Engineering & College of Flexible Electronics (Future Technology), Nanjing University of Posts & Telecommunications (NUPT), Nanjing 210023, China;  orcid.org/0000-0002-3742-4072

Longlu Wang – College of Electronic and Optical Engineering & College of Flexible Electronics (Future Technology),

Nanjing University of Posts & Telecommunications (NUPT), Nanjing 210023, China

Yuhui Feng – State Key Laboratory of Flexible Electronics (LoFE) & Institute of Advanced Materials (IAM), Nanjing University of Posts & Telecommunications (NUPT), Nanjing 210023, China

Fieifei Lin – State Key Laboratory of Flexible Electronics (LoFE) & Institute of Advanced Materials (IAM), Nanjing University of Posts & Telecommunications (NUPT), Nanjing 210023, China

Yuzhe Chen – State Key Laboratory of Flexible Electronics (LoFE) & Institute of Advanced Materials (IAM), Nanjing University of Posts & Telecommunications (NUPT), Nanjing 210023, China

Xiang Zou – State Key Laboratory of Flexible Electronics (LoFE) & Institute of Advanced Materials (IAM), Nanjing University of Posts & Telecommunications (NUPT), Nanjing 210023, China

Xiaoyuan Jia – State Key Laboratory of Flexible Electronics (LoFE) & Institute of Advanced Materials (IAM), Nanjing University of Posts & Telecommunications (NUPT), Nanjing 210023, China

Mengyue Jiang – State Key Laboratory of Flexible Electronics (LoFE) & Institute of Advanced Materials (IAM), Nanjing University of Posts & Telecommunications (NUPT), Nanjing 210023, China

Wen Lv – State Key Laboratory of Flexible Electronics (LoFE) & Institute of Advanced Materials (IAM), Nanjing University of Posts & Telecommunications (NUPT), Nanjing 210023, China;  orcid.org/0009-0004-7506-6204

Shujuan Liu – State Key Laboratory of Flexible Electronics (LoFE) & Institute of Advanced Materials (IAM), Nanjing University of Posts & Telecommunications (NUPT), Nanjing 210023, China

Complete contact information is available at:
<https://pubs.acs.org/10.1021/acssensors.Sc01118>

Author Contributions

W.Z. and Q.Z. conceived the idea for this work and supervised the project. N.D. contributed to the synthesis work, measurements, theoretical calculations, and application study. S.W. and L.W. provided theoretical guidance and supervised the computational framework. Z.Y., Y.F., F.L., X.J., and W.L. carried out the device fabrication and characterization. Y.B., Y.C., X.Z., M.J., and S.L. performed sensing characterization experiments. All authors contributed to analyzing the data.

Notes

The authors declare no competing financial interest.

■ ACKNOWLEDGMENTS

This work was supported by the National Natural Science Foundation of China (62174086 (W.Z.), 62474096 (W.Z.), 62288102 (Q.Z.) and 62404113 (Y.B.)), Outstanding Youth Foundation of Jiangsu Province (BK20240139 (W.Z.)), Basic Research Program of Jiangsu (BK20243057 (Q.Z.)), Innovation Support Program (Soft Science Research) Project Achievements of Jiangsu Province (BK20231514 (Q.Z.)), Qinglan Project of Jiangsu Province of China (W.Z.), and Postgraduate Research & Practice Innovation Program of Jiangsu Province (KYCX23_0985 (X.Z.)).

■ REFERENCES

- (1) Shi, X.; Zuo, Y.; Zhai, P.; Shen, J.; Yang, Y.; Gao, Z.; Liao, M.; Wu, J.; Wang, J.; Xu, X.; et al. Large-area display textiles integrated with functional systems. *Nature* **2021**, *591* (7849), 240–245.
- (2) Liu, W.; Zhang, C.; Alessandri, R.; Diroll, B. T.; Li, Y.; Liang, H.; Fan, X.; Wang, K.; Cho, H.; Liu, Y.; et al. High-efficiency stretchable light-emitting polymers from thermally activated delayed fluorescence. *Nat. Mater.* **2023**, *22* (6), 737–745.
- (3) Wang, W.; Jiang, Y.; Zhong, D.; Zhang, Z.; Choudhury, S.; Lai, J.; Gong, H.; Niu, S.; Yan, X.; Zheng, Y.; et al. Neuromorphic sensorimotor loop embodied by monolithically integrated, low-voltage, soft e-skin. *Science* **2023**, *380* (6646), 735–742.
- (4) Kim, Y.; Suh, J. M.; Shin, J.; Liu, Y.; Yeon, H.; Qiao, K.; Kum, H. S.; Kim, C.; Lee, H. E.; Choi, C.; et al. Chip-less wireless electronic skins by remote epitaxial freestanding compound semiconductors. *Science* **2022**, *377* (6608), 859–864.
- (5) Wu, W.; Xiao, Y.; Li, M.; Wei, Z.; Long, H.; Shen, G. A flexible bimodal self-powered optoelectronic skin for comprehensive perception of multiplexed sensing signals. *Nano Energy* **2024**, *125*, No. 109593.
- (6) Li, C.; Liu, D.; Xu, C.; Wang, Z.; Shu, S.; Sun, Z.; Tang, W.; Wang, Z. L. Sensing of joint and spinal bending or stretching via a retractable and wearable badge reel. *Nat. Commun.* **2021**, *12* (1), 2950.
- (7) Huang, H.; Dong, Y.; Wan, S.; Shen, J.; Li, C.; Han, L.; Dou, G.; Sun, L. A transient dual-type sensor based on MXene/cellulose nanofibers composite for intelligent sedentary and sitting postures monitoring. *Carbon* **2022**, *200*, 327–336.
- (8) Vermander, P.; Mancisidor, A.; Cabanes, I.; Perez, N.; Torres-Unda, J. Intelligent sitting posture classifier for wheelchair users. *IEEE Trans. Neural. Syst. Rehabil. Eng.* **2023**, *31*, 944–953.
- (9) Vukicevic, A. M.; Macuzic, I.; Mijailovic, N.; Peulic, A.; Radovic, M. Assessment of the handcart pushing and pulling safety by using deep learning 3D pose estimation and IoT force sensors. *Expert Syst. Appl.* **2021**, *183*, No. 115371.
- (10) Lu, Y.; Yang, G.; Wang, S.; Zhang, Y.; Jian, Y.; He, L.; Yu, T.; Luo, H.; Kong, D.; Xianyu, Y.; et al. Stretchable graphene-hydrogel interfaces for wearable and implantable bioelectronics. *Nat. Electron.* **2024**, *7*, 51–65.
- (11) Yang, J.; An, J.; Sun, Y.; Zhang, J.; Zu, L.; Li, H.; Jiang, T.; Chen, B.; Wang, Z. L. Transparent self-powered triboelectric sensor based on PVA/PA hydrogel for promoting human-machine interaction in nursing and patient safety. *Nano Energy* **2022**, *97*, No. 107199.
- (12) Zhang, J.; Wan, L.; Gao, Y.; Fang, X.; Lu, T.; Pan, L.; Xuan, F. Highly stretchable and self-healable MXene/polyvinyl alcohol hydrogel electrode for wearable capacitive electronic skin. *Adv. Electron. Mater.* **2019**, *5* (7), No. 1900285.
- (13) Yi, Y.; Chen, X.; Feng, S.; Chen, B.; Lu, C.; Zhou, Z. Phase separation-regulated fabrication of MXene/PVA cryogel sensor with effective electromagnetic interference shielding. *Compos. A Appl. Sci. Manuf.* **2023**, *175*, No. 107793.
- (14) Zhang, Y. Z.; El-Demellawi, J. K.; Jiang, Q.; Ge, G.; Liang, H.; Lee, K.; Dong, X.; Alshareef, H. N. MXene hydrogels: fundamentals and applications. *Chem. Soc. Rev.* **2020**, *49* (20), 7229–7251.
- (15) Gu, G.; Chen, X.; Wei, G.; Xu, M. MXene-reinforced bioactive polymer hydrogels for biomedical applications. *APL Mater.* **2024**, *12* (8), No. 080602.
- (16) Chen, X.; Zhao, Y.; Li, L.; Wang, Y.; Wang, J.; Xiong, J.; Du, S.; Zhang, P.; Shi, X.; Yu, J. MXene/Polymer nanocomposites: Preparation, properties, and applications. *Polym. Rev.* **2021**, *61* (1), 80–115.
- (17) Yu, W.; Chen, W.; Yuan, W.; Li, G.; Meng, C.; Guo, S. Ultrathin and highly-stable rubber electrodes based on island-bridge multi-filler conductive network for multilayer-Stacked dielectric elastomer artificial muscles. *Chem. Eng. J.* **2024**, *493*, No. 152714.
- (18) Kayser, L. V.; Lipomi, D. J. Stretchable conductive polymers and composites based on PEDOT and PEDOT:PSS. *Adv. Mater.* **2019**, *31* (10), No. 1806133.
- (19) Lang, U.; Müller, E.; Naujoks, N.; Dual, J. Microscopical investigations of PEDOT:PSS thin films. *Adv. Funct. Mater.* **2009**, *19* (8), 1215–1220.
- (20) Feig, V. R.; Tran, H.; Lee, M.; Liu, K.; Huang, Z.; Beker, L.; Mackanic, D. G.; Bao, Z. An electrochemical gelation method for patterning conductive PEDOT:PSS hydrogels. *Adv. Mater.* **2019**, *31* (39), No. 1902869.
- (21) Song, D.; Li, X.; Jang, M.; Lee, Y.; Zhai, Y.; Hu, W.; Yan, H.; Zhang, S.; Chen, L.; Lu, C.; et al. An ultra-thin MXene film for multimodal sensing of neuroelectrical signals with artifacts removal. *Adv. Mater.* **2023**, *35* (48), No. 2304956.
- (22) Liu, R.; Miao, M.; Li, Y.; Zhang, J.; Cao, S.; Feng, X. Ultrathin biomimetic polymeric $Ti_3C_2T_x$ MXene composite films for electromagnetic interference shielding. *ACS Appl. Mater. Interface* **2018**, *10* (51), 44787–44795.
- (23) Cheng, C.; Zhang, J.; Zhu, B.; Liang, G.; Zhang, L.; Yu, J. Verifying the charge-transfer mechanism in S-scheme heterojunctions using femtosecond transient absorption spectroscopy. *Angew. Chem., Int. Ed.* **2023**, *62* (8), No. e202218688.
- (24) Li, Y.; Gu, Y.; Qian, S.; Zheng, S.; Pang, Y.; Wang, L.; Liu, B.; Liu, S.; Zhao, Q. An injectable, self-healable, and reusable PEDOT:PSS/PVA hydrogel patch electrode for epidermal electronics. *Nano Research* **2024**, *17* (6), 5479–5490.
- (25) Liu, Q.; Qiu, J.; Yang, C.; Zang, L.; Zhang, G.; Sakai, E. High-performance PVA/PEDOT:PSS hydrogel electrode for all-gel-state flexible supercapacitors. *Adv. Mater. Technol.* **2020**, *6* (1), No. 2000919.
- (26) Yanase, I.; Ogawara, R.; Kobayashi, H. Synthesis of boron carbide powder from polyvinyl borate precursor. *Mater. Lett.* **2009**, *63* (1), 91–93.
- (27) Li, X.; Ma, X.; Zhang, H.; Xue, N.; Yao, Q.; He, T.; Qu, Y.; Zhang, J.; Tao, X. Ambient-stable MXene with superior performance suitable for widespread applications. *Chem. Eng. J.* **2023**, *455*, No. 140635.
- (28) Shi, W.; Wang, Z.; Song, H.; Chang, Y.; Hou, W.; Li, Y.; Han, G. High-sensitivity and extreme environment-resistant sensors based on PEDOT:PSS@PVA hydrogel fibers for physiological monitoring. *ACS Appl. Mater. Interface* **2022**, *14* (30), 35114–35125.
- (29) Liao, H.; Guo, X.; Wan, P.; Yu, G. Conductive MXene nanocomposite organohydrogel for flexible, healable, low-temperature tolerant strain sensors. *Adv. Funct. Mater.* **2019**, *29* (39), No. 1904507.
- (30) Hong, S.; Park, T.; Lee, J.; Ji, Y.; Walsh, J.; Yu, T.; Park, J. Y.; Lim, J.; Benito Alston, C.; Solorio, L.; et al. Rapid self-healing hydrogel with ultralow electrical hysteresis for wearable sensing. *ACS Sens.* **2024**, *9* (2), 662–673.
- (31) Zhang, H.; Li, W. X.; Tang, S.; Chen, Y.; Lan, L. M.; Li, S.; Xiong, M.; Hu, X.; Liu, Y. H.; Sun, J.; et al. A boron-based probe driven theranostic hydrogel dressing for visual monitoring and matching chronic wound healing. *Adv. Funct. Mater.* **2023**, *33* (51), No. 2305580.
- (32) Severin, I. C. Head posture monitor based on 3 IMU sensors: Consideration toward healthcare application. In the *2020 International Conference on e-Health and Bioengineering (EHB)*; IEEE: Iasi, Romania, 29–30 Oct. 2020, 1–4.
- (33) Zhao, W.; Peng, J.; Wang, W.; Jin, B.; Chen, T.; Liu, S.; Zhao, Q.; Huang, W. Interlayer hydrogen-bonded metal porphyrin frameworks/MXene hybrid film with high capacitance for flexible all-solid-state supercapacitors. *Small* **2019**, *15* (18), No. 1901351.